



Regulating the interfacial electronic coupling of PtNi/TiO₂ via bond evolution for highly efficient hydrogenation of 5-hydroxymethylfurfural

Entian Cui^a, Qingping Li^a, Xiang Wang^a, Ning Xu^c, Feng Zhang^a, Guihua Hou^a, Minghua Xie^a, Zhengchao Wang^b, Xiuli Yang^{a,*}, Yajun Zhang^{b,*}

^a Key Laboratory for Advanced Technology in Environmental Protection of Jiangsu Province, Yancheng Institute of Technology, Yancheng, Jiangsu 224051, China

^b State Key Laboratory for Oxo Synthesis & Selective Oxidation, National Engineering Research Center for Fine Petrochemical Intermediates, Lanzhou Institute of Chemical Physics, CAS, Lanzhou, Gansu 730000, China

^c Department of Physics, Yancheng Institute of Technology, Yancheng 224051, China

ARTICLE INFO

Keywords:

Photocatalysis
Interfacial electronic coupling
Bond evolution
5-hydroxymethylfurfural hydrogenation
PtNi/TiO₂

ABSTRACT

Solar-driven photocatalytic hydrogenation of 5-hydroxymethylfurfural (HMF) in the aqueous solution to form 2,5-dihydroxymethylfuran (DHMF) is an environmentally friendly method to produce fine chemical products. Herein, we demonstrate that a bimetallic PtNi-decorated TiO₂ photocatalyst (PtNi/TiO₂) exhibits excellent catalytic activity for selective HMF hydrogenation. Specifically, compared with the low conversion of Pt/TiO₂ (1.56%) and Ni/TiO₂ (0%), an HMF conversion efficiency of 100% and a DHMF selectivity of 99.7% are achieved on PtNi/TiO₂ under mild conditions. The detailed structure and in-situ characterizations first reveal the strong electronic coupling between PtNi alloy and TiO₂, which not only effectively promotes charge migration but also undergoes the evolution of surface chemical bonds during the photocatalytic HMF process. Furthermore, the significantly enhanced η²-(C, O) aldehyde adsorption configuration of HMF molecules to form DHMF via the CH-O-immediate route is also evidenced. This work provides a new insight for designing and fabricating highly efficient photocatalysts for HMF selective hydrogenation.

1. Introduction

5-Hydroxymethylfurfural (HMF) is a key platform compound for the production of fine chemicals and sustainable fuels [1–4]. The selective hydrogenation of HMF to symmetric 2,5-dihydroxymethylfuran (DHMF) is highly desired for its potential application in producing ethers, polymers, etc [4–6]. Unlike traditional thermocatalysis technology with harsh reaction conditions [7–10], photocatalytic HMF hydrogenation can be performed at room temperature and atmospheric pressure [11]. For example, Pt/g-C₃N₄ has been shown to successfully photocatalytic HMF hydrogenation to DHMF at room temperature under visible light irradiation [12]. The HMF conversion and DHMF yield over a Pd/MIL-101(Fe)-NH₂ photocatalyst reached 35% and 27%, respectively [13]. Although photocatalysis is a mild and economical route for HMF conversion, the relatively poor selectivity of target products still remains in the present semiconductor-based photocatalytic system [14,15], especially in the presence of water solution.

Recently, various strategies have been developed to improve the photocatalytic selectivity of the target product. Using anhydrous ethanol

as the reaction medium and hydrogen donor, the HMF conversion and DHMF selectivity over the amorphous TiO₂ photocatalyst both reached > 99% [16]. When the Pd active sites were protected with a thin carbon shell, the WO₃/PdOx@C photocatalyst achieved a high conversion efficiency (>95%) of HMF and exhibited 79.2% selectivity for DHMF [17]. The Au/SiC photocatalysts with a space charge zone established at the metal-semiconductor interface could effectively photocatalytic HMF into DHMF, with 90% conversion and 93% selectivity. The electron enrichment effect and steric effects at the interface favored the preferential adsorption of HMF for selective conversion to DHMF [18,19]. Accordingly, it is clear that a highly efficient HMF hydrogenation photocatalyst must simultaneously possess three characteristics: 1) rapid electron transfer to active sites; 2) sufficient protons supply for HMF hydrogenation; and 3) the adsorption configuration of HMF molecules to improve the product selectivity. Although great efforts have been made in the burgeoning research to improve the activity and selectivity of HMF conversion in the photocatalytic process, the fundamental understanding of interfacial electronic and bond structure characteristics under the excited state between cocatalyst and semiconductor,

* Corresponding authors.

E-mail addresses: xyang@ycit.edu.cn (X. Yang), yajunzhang@licp.cas.cn (Y. Zhang).

<https://doi.org/10.1016/j.apcatb.2023.122560>

Received 12 November 2022; Received in revised form 24 January 2023; Accepted 2 March 2023

Available online 5 March 2023

0926-3373/© 2023 Elsevier B.V. All rights reserved.

especially for bimetallic cocatalysts, has been rarely concerned until now (Table S1).

Herein, by taking bimetallic PtNi-decorated TiO₂ (PtNi/TiO₂) as the catalyst model, we first demonstrate that PtNi/TiO₂ can significantly promote the conversion of HMF into DHMF with 100% conversion and 99.7% selectivity, owing to the strong electronic coupling between PtNi cocatalysts and TiO₂. Benefitting from the interfacial bonding for Pt-O and Ni-O bond, PtNi/TiO₂ exhibits effectively facilitate the photoinduced electron transfer from TiO₂ to PtNi active sites and modulate the PtNi electronic structure to optimize the adsorption HMF configuration. Therefore, modulation of the electronic structure of the active metal and interface metal-semiconductor interaction is an alternative strategy for promoting photocatalytic HMF conversion and DHMF formation.

2. Experimental sections

2.1. Materials and reagents

Tetrabutyl titanate, Nafion solution, ethylene glycol, platinum (II) acetylacetonate and nickel acetate tetrahydrate were purchased from J&K Scientific Ltd, China. 5-Hydroxymethylfurfural, 2,5-dihydroxymethylfuran, and isopropyl alcohol were supplied by Shanghai Macklin Biochemical Technology Co., Ltd, China. Methanol and absolute ethanol were purchased from Sinopharm Chemical Reagent Co. Ltd, SCRC, China. Deionized water (Molecular Corp., 18.25 MΩ cm⁻²) used in the synthesis was from local sources.

2.2. Preparation of TiO₂ nanosheets

The TiO₂ nanosheets were prepared according to the previous reference [20].

2.3. Preparation of (1 wt%) Pt/TiO₂

200 mg TiO₂ and 40 mL ethylene glycol were added into a 150 mL round-bottom flask and stirred the mixture vigorously for 30 min. And then, 41 mg platinum (II) acetylacetonate (Pt(acac)₂) was added into the above mixture. After stirring for another 30 min, the round-bottom flask was placed in an oil bath pot and pump argon gas into the flask for 40 min to drive the air out of the flask. After reacting at 150 °C for 12 h, washing the product three times with ethanol and water mixture (V: V=1:1) and drying it in a vacuum at 30 °C.

2.4. Preparation of (1 wt%) PtNi/TiO₂ series samples

The synthesis procedure was similar to that of (1 wt%) Pt/TiO₂ with 41 mg Pt(acac)₂ replaced by the mixture of Pt(acac)₂ and nickel acetate tetrahydrate with different atomic ratios (Pt_{0.9}Ni_{0.1}, Pt_{0.8}Ni_{0.2}, Pt_{0.7}Ni_{0.3}, Pt_{0.6}Ni_{0.4}, and Pt_{0.5}Ni_{0.5}).

2.5. Characterizations

The morphological characteristics were observed on transmission electron microscopy (JEOL JEM-2100 F). The X-ray diffraction (XRD) characterization was carried out on the X-ray diffractometer (Rigaku B/Max-RB, Cu Kα radiation). The scientific ESCALAB250i-XPS photoelectron spectrometer was used to record X-ray photoelectron spectroscopy (XPS) spectra and synergism illumination XPS (SI-XPS). The specific surface area was determined by Micromeritics ASAP 2020 M. Photoluminescence spectra (PL) were obtained on a steady-state Fluorescence Spectrometer (FluoroMax-4). The Fourier transform infrared spectrometer (FTIR) test was implemented on Nexus 670 Nicolet. UV-Vis DRS characterization was implemented on a HITACHI U-3310 spectrophotometer. The fluorescence decay processes were recorded on an Edinburgh FLS920 phosphorescence system at normal atmospheric temperature.

In-situ Fourier-transform infrared spectroscopy (ATR-FTIR) of HMF adsorption was performed using a Bruker Tensor 27 FTIR spectrometer with an MCT detector. The sample was loaded into a cell from HARRIC. Each spectrum was recorded with 32 scans at a resolution of 4 cm⁻¹ under light irradiation.

X-ray adsorption near edge structure (XANES) measurements at Pt L₃-edge of TiO₂, Pt/TiO₂, and PtNi/TiO₂ samples were measured at Shanghai Synchrotron Radiation Facility in China. The output beam was selected by Si (111) monochromator. The energy was calibrated by Pt foil. The data were collected at room temperature under fluorescence mode by using the solid-state detector.

2.6. Photocatalytic performance evaluation

All the experiments were carried out in a home-made photochemical reactor under Ar atmosphere. During the photocatalytic process, water was circulated to maintain the reactor temperature at 30 °C. As-synthesized samples (50 mg), HMF solution (100 mL, 5 mmol L⁻¹) and CH₃OH (25 mL) were added into a 200 mL quartz reactor. The reactor was evacuated and purged with Ar for 40 min. The reaction mixture was stirred at 650 rpm and irradiated under 300 W Xe lamp (λ = 320–780 nm). After the reaction, the solid catalyst was filtered. The liquid products were analyzed by HPLC (Agilent 1200) using a C18 column and a UV detector, and the gas products were detected by GC (Agilent 8860) equipped TCD and FID detectors.

The rate constant of the reaction was determined at four different temperatures (0, 20, 30, and 40 °C). From the slope of the plot of lnK vs 1/T. The reaction activation energy (E_a) was determined (E_a = -slope/R).

2.7. Photoelectrochemical tests

The photoelectrochemical tests were carried out on CHI660E electrochemical workstation with a Pt counter electrode and an Ag/AgCl reference electrode, respectively. All data were converted into standard hydrogen electrode potential.

The working electrode was prepared as following procedure: 1) to avoid direct contact between cocatalyst (Pt, PtNi) and glassy carbon, the electrodes were firstly modified by TiO₂ thin film. 3 mg TiO₂ was firstly dispersed into 1 mL ethanol and 50 μL Nafion solution (10 wt%) under sonication for 30 min, and then 4 μL of the resulting solution was dropped onto an L-glassy carbon electrode and dried at room temperature. 2) the as-synthesized photocatalysts were deposited onto TiO₂ film. 5 mg as-synthesized photocatalysts were dispersed into 1 mL ethanol and 50 μL Nafion solution (10 wt%) under sonication for 30 min. After that, 5 μL of the resulting dispersion was dropped onto TiO₂ film-coated glassy carbon electrode and dried at room temperature.

2.8. Calculation

Density functional theory (DFT) calculations were carried out using the Cambridge Serial Total Energy Package. The exchange-correlation energy was described using the revised Perdew-Burke-Ernzerh of exchange-correlation density functional (PBESOL) within the generalized-gradient approximation (GGA). A 400 eV plane-wave kinetic energy cutoff was chosen. The Brillouin zone was sampled with 6 × 6 × 7, 1 × 1 × 1 Monkhorst-Pack grids, respectively, for TiO₂ bulk and surfaces calculations. A 3 × 5 × 1 supercell was generated for neglecting intermolecular interactions at the surface. This model shows a 15.1 × 20.7 Å² surface. The atomic positions were fully relaxed until a maximum energy difference and residual force on atoms, respectively, converged to 10⁻⁵ eV and 0.03 eV Å⁻¹. A 15 Å thick vacuum layer was used to avoid the interaction between the top and bottom surfaces.

3. Results and discussions

3.1. Structure and photocatalytic performance determinations

Transmission electron microscopy (TEM) images (Fig. 1a, S1 and S2) of as-prepared catalysts clearly show uniform nanoparticles with a size in the range of 4–10 nm have been dispersed on the edge of TiO₂ nanosheets. The energy dispersive spectroscopy (EDS) elemental line scanning (Fig. 1b) and elemental mapping images (Fig. 1c and d) reveal the existence of Pt and Ni elements in the as-prepared nanosheet, indicating the successful preparation of Pt/TiO₂, Ni/TiO₂ and PtNi/TiO₂. X-ray diffraction (XRD, Fig. S3) result further indicates all the diffraction peaks of as-prepared catalysts can be indexed to the tetragonal structure of TiO₂ (JCPDS No. 004–0477) [21], while no evident diffraction peaks corresponding to Pt, Ni and PtNi cocatalysts can be detected, mainly originating from its low content (1 wt%) and high dispersion.

Subsequently, the photocatalytic HMF hydrogenation performance for the bare TiO₂, Pt/TiO₂, Ni/TiO₂ and PtNi/TiO₂ series samples was evaluated under full-spectrum irradiation ($\lambda = 320\text{--}780\text{ nm}$) using High-performance liquid chromatography (HPLC) (Table S2). More specifically, the adsorption range of HMF is 230–300 nm, with a maximal intensity at approximately 284 nm, and the retention times of HMF and DHMF in HPLC are determined by the respective standards (Fig. S4), and the HMF concentration in the photocatalytic system is determined by the external standard method [22]. Before HMF hydrogenation, the photocatalytic hydrogen production ability in the methanol system has been first explored. As shown in Fig. S5, the hydrogen yields in 5 h of Pt/TiO₂, Ni/TiO₂ and PtNi/TiO₂ catalysts are 595.8

μmol , 38 μmol and 207.2 μmol , respectively. By contrast, with HMF addition under the ground state, no products for H₂ and DHMF are detected in all reaction systems. Under light irradiation, no or trace amounts of H₂ and DHMF products are detected in the bare TiO₂, Ni/TiO₂ and Pt/TiO₂ in the HMF solution system, respectively. Amazingly, a drastic increase in both hydrogen evolution and DHMF selectivity is observed in the series PtNi/TiO₂ catalysts, indicating that the decoration of PtNi cocatalysts on TiO₂ nanosheets can significantly promote HMF hydrogenation activity (Fig. 2a and Table S2). In particular, an outstanding yield of H₂ (24.8 μmol) and DHMF (498.3 μmol) and superior HMF conversion efficiency (100%) have been obtained in the Pt_{0.8}Ni_{0.2}/TiO₂ (Fig. 2b). Herein, the Pt_{0.8}Ni_{0.2}/TiO₂ is simplified as PtNi/TiO₂. Moreover, the above results further indicate that the strong adsorption of HMF on the bimetallic activity site, prevents hydrogen evolution from water splitting. Except for the high conversion efficiency, the high selectivity (99.7%) for DHMF is also achieved over PtNi/TiO₂. Meanwhile, the photocatalytic HMF hydrogenation over Pt_{0.8}Ni_{0.2}-decorated amorphous TiO₂ (Pt_{0.8}Ni_{0.2}/a-TiO₂) was also performed and shown in Fig. S6. The conversion of HMF (94.2%) and selectivity of DHMF (79.5%) are obtained in Pt_{0.8}Ni_{0.2}/a-TiO₂, which are lower than these of the PtNi/TiO₂ system, attributing to the high crystalline and two-dimensional sheet structure of TiO₂. Moreover, the products of methanol after the reaction have also been investigated. As shown in Fig. S7, HCHO is the only liquid product for methanol oxidation over PtNi/TiO₂ (Fig. S7a and b), accompanied by a track amount of CO₂ (Fig. S7c), indicating that the relatively weak oxidation ability of as-prepared PtNi/TiO₂ catalysts. The photocatalytic stability of PtNi/TiO₂ for HMF hydrogenation was explored by cycling experiment. As

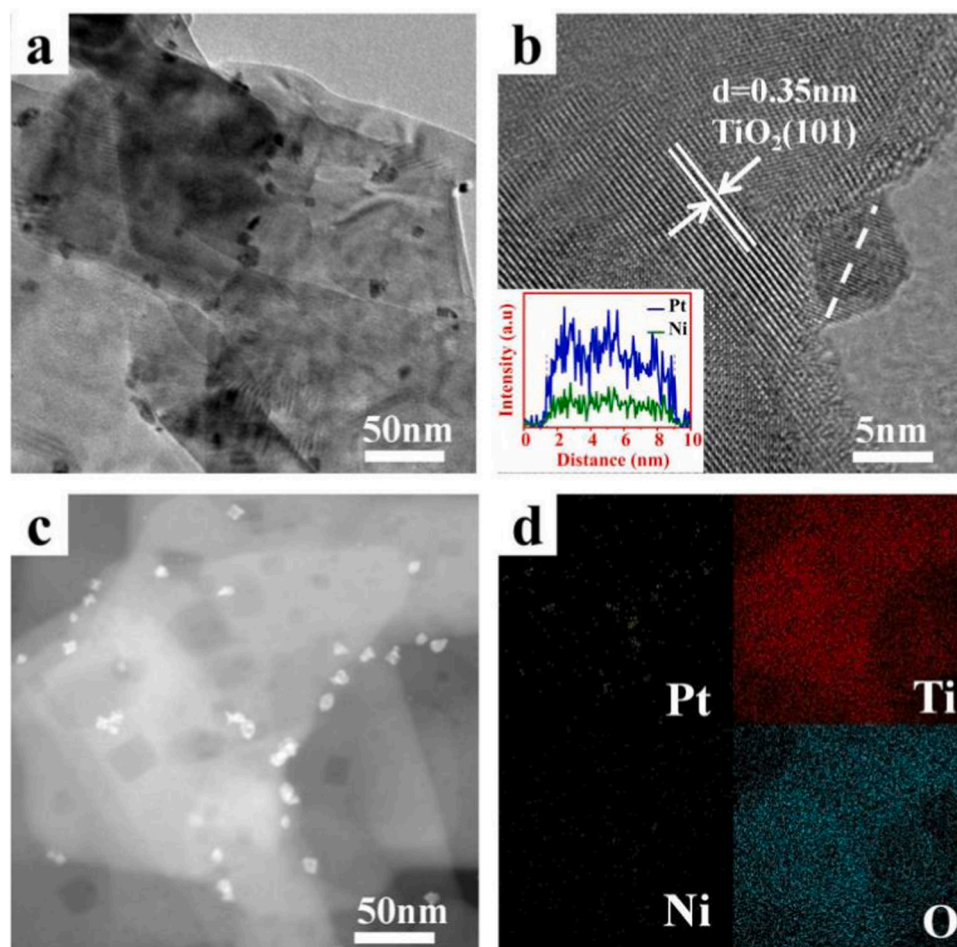


Fig. 1. Representative TEM (a), HRTEM (line-scan Pt and Ni element) (b), HAADF-STEM (c), and mapping-scan elemental profiles (d) of PtNi/TiO₂ catalyst.

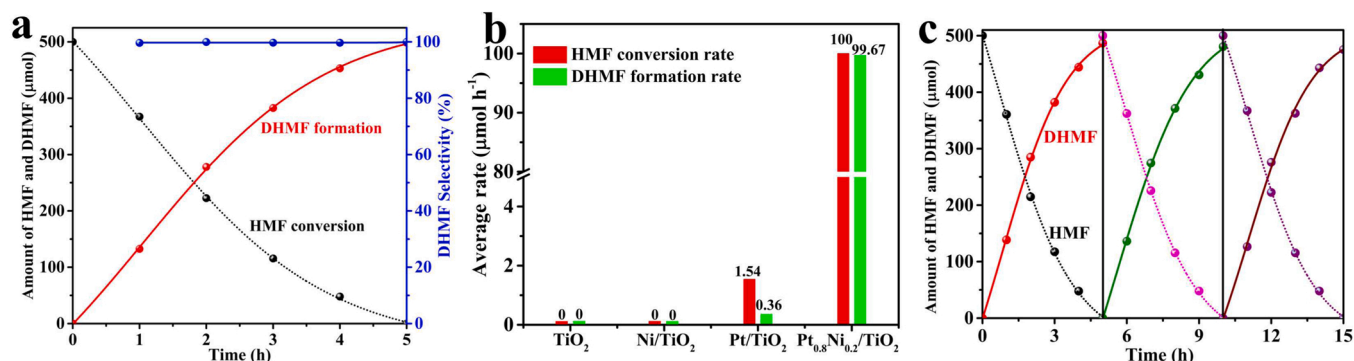


Fig. 2. (a) Time courses of photocatalytic HMF hydrogenation for Pt_{0.8}Ni_{0.2}/TiO₂ catalysts; (b) Comparative presentation of the HMF conversion and DHMF formation rate for different catalysts; (c) Cycling stability of PtNi/TiO₂ catalysts for HMF hydrogenation and DHMF formation.

shown in Fig. 2c, the PtNi/TiO₂ catalyst can generally keep its original activity even after three cycles, indicating its excellent photostability for HMF hydrogenation. Additionally, UV–vis diffuse reflectance spectra (UV–vis DRS, Fig. S8a) and Nitrogen adsorption/desorption analysis (Fig. S8b) reveal that after the modification of PtNi alloy on the TiO₂ surface, no evident change in photoabsorption properties and specific surface area can be detected compared with bare TiO₂ nanosheet catalysts, which further confirm the crucial roles of PtNi alloy cocatalysts.

Reaction condition: 50 mg catalysts, HMF solution (100 mL, 5 mmol L⁻¹), pure methanol (25 mL); Reaction time: 5 h.

To clearly clarify the effect of real reductants in the photocatalytic HMF hydrogenation process, a series of control experiments (e.g., pure water, hydrogen gas and methanol solution (20 vol%)) have been performed and shown in Table 1. Under the ground state, no product for DHMF is detected over PtNi/TiO₂ catalysts in pure water, the hydrogen atmosphere, methanol solution, and hydrogen and methanol mixture system, respectively, owing to the absence of energy (e.g., heat or light) to drive the reaction to occur [13,16,23]. Upon the light irradiation, the significantly enhanced HMF conversion and DHMF selectivity are obtained over PtNi/TiO₂ in the methanol solution as well as in the hydrogen and methanol mixture system, indicating the light excitation can significantly affect the HMF hydrogenation activity. Moreover, these results further indicate that the proton production from methanol oxidation in the methanol system is more favorable for the HMF conversion to DHMF (99.7%) in comparison with the selectivity (99.5%) of the hydrogen and methanol mixture system. Moreover, the effect of ethanol and isopropanol in HMF hydrogenation over PtNi/TiO₂ has been also investigated. As shown in Fig. S9, the conversion efficiencies of HMF over PtNi/TiO₂ are nearly 100% in ethanol and isopropanol systems, respectively, and the slightly lower selectivity of DHMF in ethanol (99.2%) and isopropanol (98.3%) systems are obtained in comparison with that of methanol system (99.7%), indicating the methanol is more easily oxidized by the PtNi/TiO₂ catalysts to provide protons in comparison with ethanol and isopropanol.

To disclose the detailed structural and coordination information of PtNi cocatalyst, X-ray absorption fine structure (XAFS) spectroscopy was

conducted. The X-ray absorption near-edge structure spectra (XANES) of Pt L₃-edge and Ni K-edge show the valence state and local structure of both Pt and Ni atoms in as-prepared catalysts (Fig. 3a and c). Detailed EXAFS fittings of the Pt L₃-edge and Ni K-edge spectra were carried out to investigate the specific structure of Pt and Ni in the PtNi/TiO₂. The Pt L₃-edge EXAFS fitting results (Fig. 2b) suggest that the peaks located at 2.12 and 2.61 Å, corresponding to Pt–Ni and Pt–Pt bonds [24], respectively, indicating that Pt forms an alloy with Ni in which the Pt–Ni intermetallic coordination is the main component of the Pt local environment. Notably, a typical peak at about 1.71 Å assigned to the Pt–O bond is detected, indicating that Pt atom formed an effective bonding interaction with oxygen atoms on the surface of TiO₂. Similar results are also obtained by the Ni K-edge fitting result of Ni–Pt and Ni–O with a bond length of 2.58 and 1.61 Å (Fig. 3d). The above results further indicate that the preparation of PtNi alloy and TiO₂ formed an effective bonding interaction.

3.2. The dynamic evolution of the interface Pt–Ni structure

To further reveal the role of PtNi cocatalyst in the catalytic process, the synchronous illumination X-ray photoelectron spectroscopy (SI-XPS) technique was performed to explore the surface chemical state and charge migration ability for HMF absorption on PtNi/TiO₂ catalysts (Fig. 4). Under the ground state (≤100 min, Fig. 4a), no significant evolution of peak is observed. Obviously, the high-value Pt species (Pt²⁺) species at 72.1 eV can be detected in Pt 4f region [25], resulting from the formation of Pt–O bonds on TiO₂ surface, which is consistent with the result of Pt XAFS [1,26]. Upon illumination, the binding energy of Pt 4f first shifted to the lower direction and then stabilized within 40 min, indicating that the electronic structure of PtNi species experienced a process from change to stability. Interestingly, the disappeared shoulder peak is assigned to the breaking of the interface Pt–O bond under the excitation states forming metallic Pt (Fig. 4b), resulting in a strong interaction between Pt species and TiO₂ [27,28]. Moreover, the Ni species in PtNi/TiO₂ under light illumination exhibits a similar change trend (Fig. 4c), in which the peak of metallic Ni is blue-shifted

Table 1
Control experiments of photocatalytic HMF hydrogenation to DHMF.

Sample	Solvent	HMF (μmol)	DHMF (μmol)	HMF (conversion) (%)	DHMF (selectivity) (%)	Light On/off
PtNi/TiO ₂	water	500	0	0	0	Off
PtNi/TiO ₂	water	500	0	0	0	On
PtNi/TiO ₂	H ₂	500	0	0	0	Off
PtNi/TiO ₂	H ₂	500	0	0	0	On
PtNi/TiO ₂	CH ₃ OH solution	500	0	0	0	Off
PtNi/TiO ₂	CH ₃ OH solution	0	498.3	100	99.7	On
PtNi/TiO ₂	H ₂ + CH ₃ OH solution	500	0	0	0	Off
PtNi/TiO ₂	H ₂ + CH ₃ OH solution	0	497.3	100	99.5	On

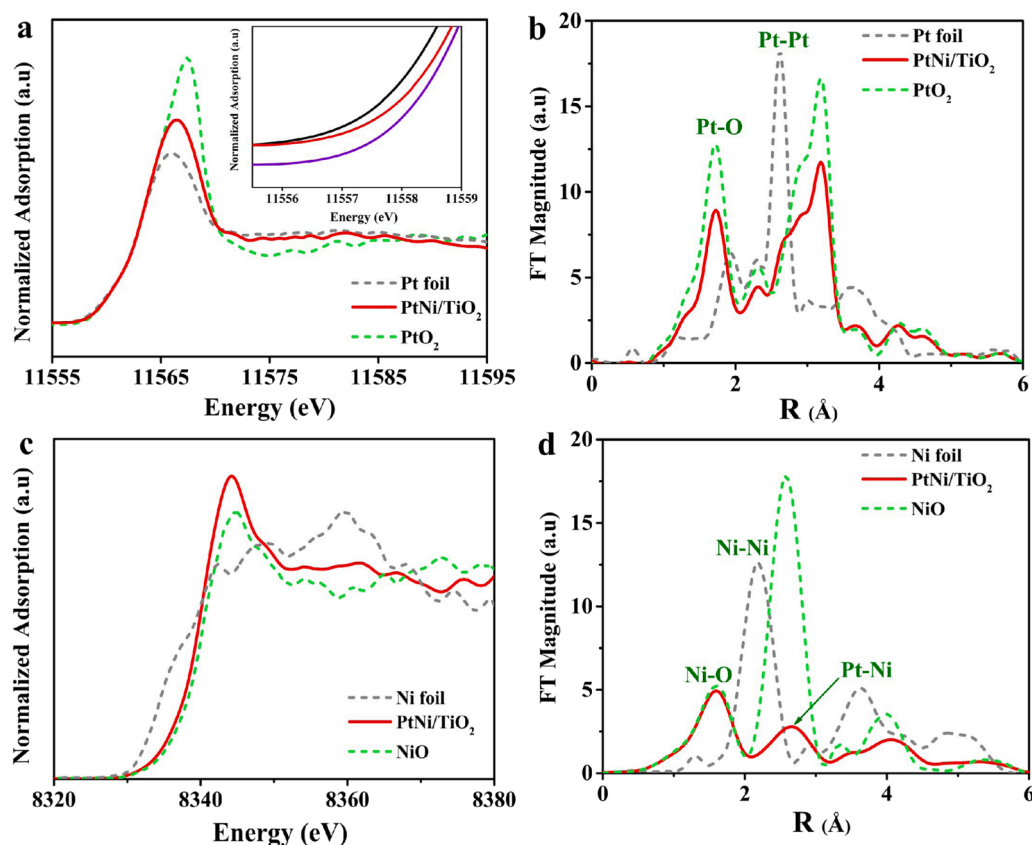


Fig. 3. Pt K-edge (a) and Ni k-edge (c) XANES spectra of PtNi/TiO₂ and the reference samples. K³-weighted Fourier transform Pt L₃-edge (b) and Ni L₃-edge (d) EXAFS spectra for PtNi/TiO₂ and the reference samples (no phase correction).

after light illumination (Fig. 4d). Above demonstrates further confirm that the PtNi alloy cocatalysts not only effectively promote the charge migration but also undergo the evolution of surface chemical bond in the photocatalytic HMF hydrogenation. Furthermore, the charge variations of Pt atoms are further verified by diffuse reflectance Fourier transform infrared spectroscopy (DRIFTS) for CO adsorption on PtNi/TiO₂ [29,30] (Fig. S10). The peak at 2035 cm⁻¹ is attributed to CO on partially negatively charged Pt (Pt^{δ-}-CO) and a redshift from the gas phase value (2100–2220 cm⁻¹) is observed, indicating an increased d-electron back-donation to the CO π* orbital from PtNi [31–33] and Pt (Pt^{δ+}) and positive Ni (Ni^{δ+}) are obtained in Fig. S11, which would influence the adsorption performance of the PtNi alloy.

3.3. Roles of interface structure in promoting the electron-hole separation

To investigate the interfacial charge transfer process between the metal and semiconductor, electrical impedance spectroscopy (EIS) measures were performed for these obtained samples [34,35]. Based on the Nyquist plots (Fig. 5a) and the fitting equivalent circuit (insert in Fig. 5a), the calculated resistance values of bare TiO₂, Pt/TiO₂, Ni/TiO₂, PtNi/TiO₂ are 181.3, 114.6, 138.5 and 95.9 Ω, respectively, indicating the preferable capability of the PtNi/TiO₂ catalyst for facilitating interfacial charge transfer. Subsequently, the photoluminescence (PL) spectra were collected to further explore the photogenerated carrier recombination. Specifically, the photoluminescence (PL) intensity of PtNi/TiO₂ sample (Fig. 5b) has been significantly decreased in comparison with other samples, indicating the high charge separation and migration efficiency by the alloy modification. Then, time-resolved photoluminescence (TR-PL) spectroscopy was employed to analyze the behavior of charge separation and recombination kinetics. The TR-PL results (Fig. 5c) reveal that the electron lifetime for PtNi/TiO₂ is 5.37 ns, higher than these of bare TiO₂ (2.95 ns), PtNi/TiO₂ (3.11 ns),

and PtNi/TiO₂ (4.58 ns). The increased lifetime and the induced PL intensity of PtNi/TiO₂ should be attributed to the efficient charge migration from TiO₂ to PtNi, which is consistent with the results of SI-XPS and EIS. The chronoamperometric i-t curves (Fig. 5d) clearly reveal that PtNi/TiO₂ exhibits superior photocurrent density, more than 8.6, 1.43, 3.52 times higher than that of bare TiO₂, Pt/TiO₂ and Ni/TiO₂, respectively. The valence band of as-prepared samples is measured by XPS valence spectra, the electron density of PtNi/TiO₂ in the lower binding energy region is much higher than other catalysts (Fig. S12), indicating that there are more electrons in PtNi/TiO₂ [36]. Based on the above results, the modification of PtNi alloy cocatalyst on TiO₂ can significantly improve the photogenerated charge separation and migration ability, which further verifies the results of the catalytic HMF.

3.4. The adsorption behavior of HMF on PtNi/TiO₂

The adsorption configuration of HMF absorption on PtNi/TiO₂ was investigated by Sum frequency generation (SFG) vibrational spectroscopy. As presented in Fig S13, there are two obvious peaks, centered at 2922 and 3137 cm⁻¹, which are ascribed to the strong aromatic feature and CH₂-symmetric stretch, respectively [37]. This result represents the furfuryl-oxy intermediate resulting from furfural dye bonding to PtNi alloy via carbonyl O atoms followed by hydrogen to carbonyl C. Subsequently, the reaction intermediates during photocatalytic HMF on PtNi/TiO₂ were carried out using in-situ Attenuated total reflection fourier transformed infrared spectroscopy (ATR-FTIR) (Fig. 6a) [38]. For furan compounds, the suitable wavenumber region is 1200–1800 cm⁻¹ [39]. The IR spectrum of pure HMF is also presented as a reference. The band center at 1678 cm⁻¹ arises from the C=O vibration [16]. The bands center at 1362, 1465, and 1554 cm⁻¹ can be assigned to the vibration of the C=C bond of the furan ring [40,41]. The band of furan ring C=C vibration (1554 cm⁻¹) does not show an

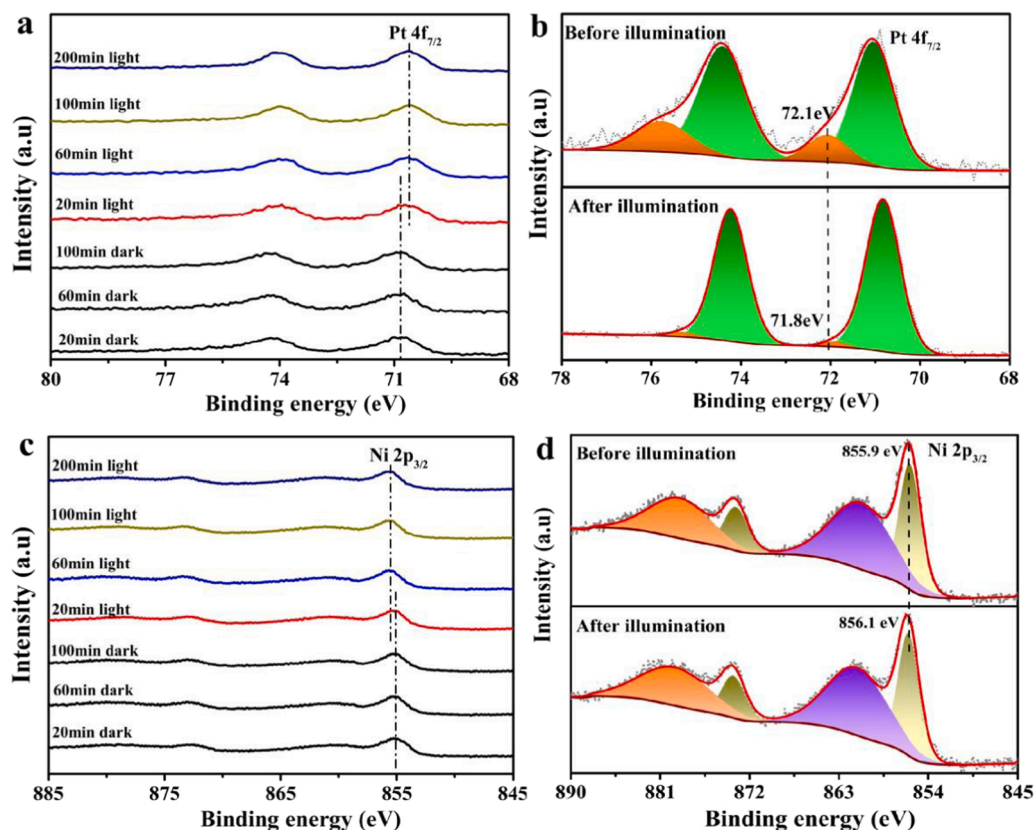


Fig. 4. SI-XPS spectra high-resolution Pt 4f (a,b) and Ni 2p (c,d) of PtNi/TiO₂.

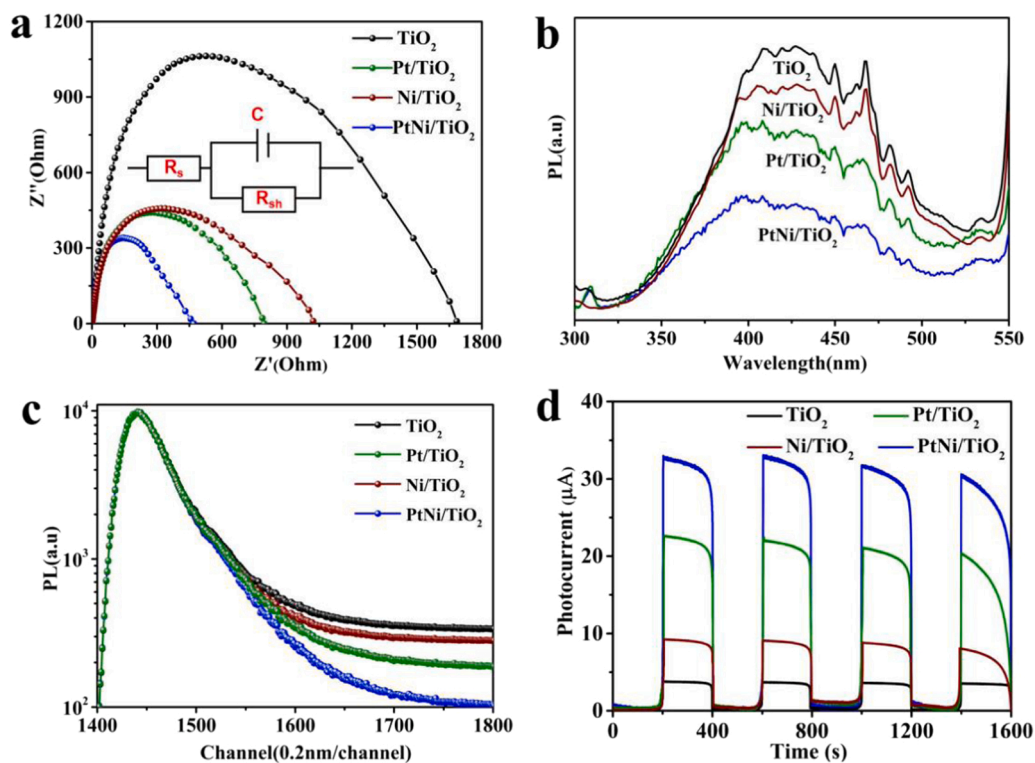


Fig. 5. Nyquist plots (a), time-integrated (b), fitted time-resolved photoluminescence spectra (c), photocurrent response (d) of as-prepared catalyst.

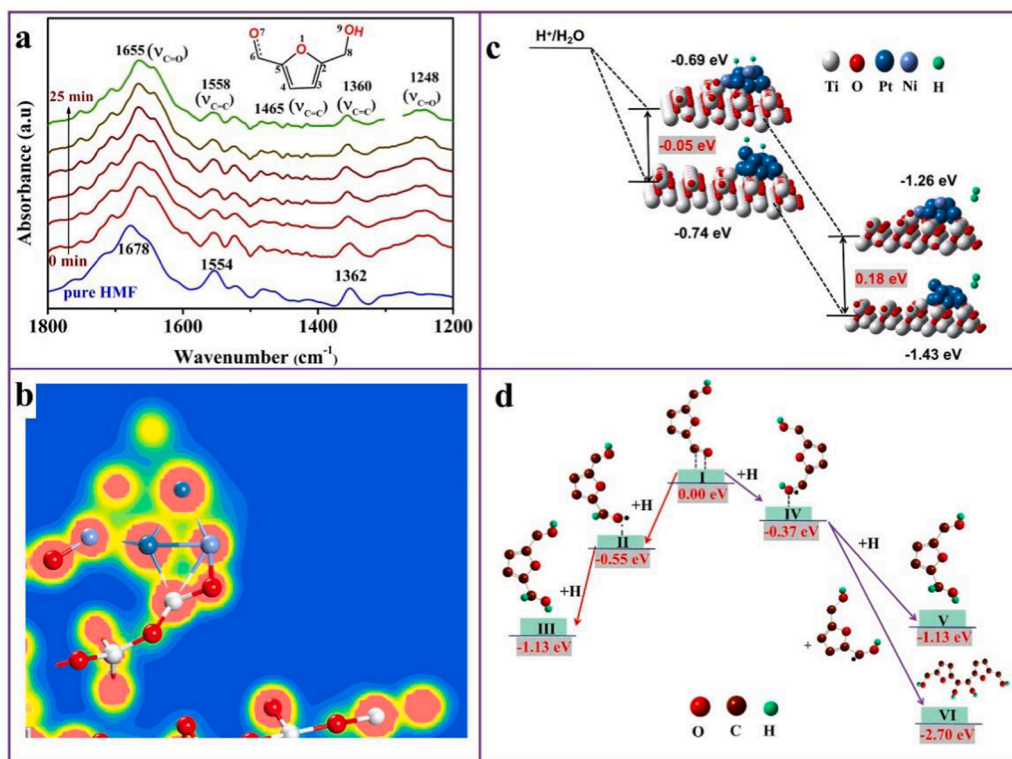


Fig. 6. (a) Time-resolved ATR-FTIR spectra of HMF absorption on PtNi/TiO₂ under light illumination; (b) electron density difference of PtNi/TiO₂; (c) energy-change profiles of proton and H₂ formation and (d) total-energy-change profiles of HMF hydrogenation over PtNi/TiO₂.

obvious shift after adsorption. After adsorption on PtNi/TiO₂, the band of furan ring C=O is blue-shifted approximately 23 cm⁻¹, indicating the interaction between the aldehyde group and PtNi alloy. Notably, a new additional band at approximately 1248 cm⁻¹ is detected, indicative of the change of aldehyde group C=O to C-O bond (more precisely, C=O with strong single bond characteristics), for the reason that the strong interaction between C=O group and PtNi alloy because the vibration peaks of C-O bonds belonging to C-O-C and C-OH in HMF are beyond 1200–1800 cm⁻¹ [42,43]. The strong interaction leads to the preferential formation of the CH-O-intermediate, resulting in the reaction between the CH-O-intermediate and in situ generated proton to form DHMF [44]. A previous report proves that on the Pt surface, the HMF molecule adsorption configuration is η²(C, O)-aldehyde, in which the C atoms and O atoms of the aldehyde group all interacted with Pt (denoted Pt...C and Pt...O), respectively [45]. Owing to the synergistic effect of the PtNi alloy and enhanced interfacial interaction of PtNi-TiO₂, the adsorption configuration of HMF on PtNi/TiO₂ is modified η²(C, O)-aldehyde with strengthened PtNi...O interactions and weakened PtNi...C interactions. On the one hand, the synergism effect modified the electronic structure of the PtNi alloy with negative Pt (Pt^{δ-}) and positive Ni (Ni^{δ+}), which can enhance the Ni(Pt)...O interaction and weaken the Pt(Ni)...C interaction; on the other hand, the high toxophilite of the Ni element is also in favor of strengthening the interaction between the PtNi alloy and the O atom of the aldehyde group. The modified adsorption configuration brought two benefits. The first is the lowered hydrogenation barrier, making the activation of the C=O group easier. The activation energy of PtNi/TiO₂ (46.5 kJ mol⁻¹) is smaller than these of bare TiO₂ (100.6 kJ mol⁻¹) and Pt/TiO₂ (89.7 kJ mol⁻¹) (Fig. S14). The second is the terminal oxygen adsorption of HMF, which repulses the methylol group and furan ring away from the PtNi surface, preventing the hydrogenation of HMF over PtNi/TiO₂ catalysts.

The electronic structure characteristics of PtNi/TiO₂ have first been explored via density functional theory (DFT). Fig. S15a presents the most stable configuration of PtNi on the TiO₂ surface with an adsorption

energy of -2.42 eV. The enhanced PtNi-TiO₂ interfacial interaction leads to a slight upward trend of the related O atoms. The new hybrid states associate with Pt result from the strong interaction between PtNi and TiO₂ (Fig. S15b), an indicator of the formation of a strong interaction between O and Pt [46–48]. The partial density of states (PDOS) of Ni is very small, but it did exist; therefore, the effect of Ni on the PtNi-TiO₂ interfacial interaction cannot be excluded. Obvious electron density accretion among Pt was detected (Fig. 6b). The interface O atoms have a smaller electron density than bulk O atoms. Moreover, there is an obvious additional ca. 0.6–0.7 electrons between interface Pt and interface O, which is more to Pt atoms, suggesting an enhanced occupation of the d states of Pt. As we know, the absorption and desorption of proton over the catalyst surface is a key factor determining the HMF conversion efficiency. As shown in Fig. 6b, the Gibbs free energy of proton absorption on PtNi/TiO₂ and Pt/TiO₂ are -0.69 and -0.74 eV, respectively (Fig. 6c), indicating the proton absorption ability over PtNi/TiO₂ is more energetically favorable than Pt/TiO₂. During the hydrogen desorption process, the Gibbs free energy for the hydrogen desorption process is -1.43 eV, confirming that hydrogen desorption ability over PtNi/TiO₂ is better than that of Pt/TiO₂ (-1.26 eV). The above results demonstrate that PtNi alloy cocatalyst can effectively promote HMF hydrogenation ability.

Subsequently, the adsorption configuration of HMF on PtNi/TiO₂ is also calculated. As stated in Fig. S16, the optimized electronic structure of the PtNi alloy results in the modified η²(C, O)-aldehyde configuration. For the HMF adsorption on PtNi/TiO₂ surface, the bond lengths of PtNi...O and PtNi...C are calculated to be 1.92 and 2.80 Å, while the bond lengths of Pt...O and Pt...C in HMF-Pt/TiO₂ system are 2.20 and 2.27 Å, respectively, which indicates the Ni atoms are the interaction sites to bind O atoms of the aldehyde group. The reaction route is studied through a total-energy-change approach, which only focuses on the energy difference among reactants, intermediates, and products [49–51]. Thus, two possible HMF hydrogenation pathways are given in Fig. 6d. (1) the addition of a proton to the C atom of the carbonyl group,

leading to the form O radical (CH-O·) (I→II); (2) the addition of a proton to the O atom of carbonyl group, forming of C radical (·C-OH) (I→IV). The formation of C-OH intermediate may be further reduced by the addition of a proton to form DHMF (IV→V) or couple with another C-OH intermediate to produce 1,10-bis(hydroxymethyl)-hydrofuroin (IV→VI). The CH-O-intermediate can only result in DHMF by the addition of another proton (II→III). The calculated formation energy of the CH-O-intermediate (I→II) is -0.55 eV, which is more favorable by 0.18 eV than that of the C-OH intermediate. The CH-O-intermediate hydrogenation to form DHMF is -1.13 eV. The above results indicate that the reduced energy barrier and HMF hydrogenation ability mainly originates from strong interfacial coupling and electron structure regulation of PtNi/TiO₂ catalyst.

3.5. The proposed photocatalytic mechanism

On the basis of the above results, a reaction mechanism for photocatalytic HMF hydrogenation over PtNi/TiO₂ is proposed, as displayed in Scheme 1. HMF molecules are bound to the PtNi alloy by a modified η^2 (C, O)-aldehyde adsorption configuration with strengthened PtNi...O interactions and weakened PtNi...C interactions. Under light illumination, the photoinduced electrons generated from TiO₂ are transferred rapidly to the PtNi alloy, owing to the enhanced PtNi-TiO₂ interfacial interaction. The photoinduced electrons reduce $\text{H}^+/\text{H}_2\text{O}$ into a proton, while the photoinduced holes are captured by CH₃OH. The electronic structure of PtNi lowers the proton recombination activity, leaving most of the proton participating in HMF reduction instead of forming H₂. The proton is bound to the O atom of the aldehyde group, forming a CH-O-intermediate, which is reacted immediately by the other H atom to form DHMF.

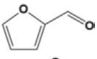
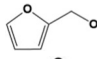
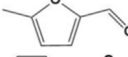
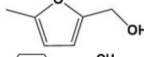
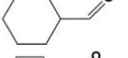

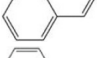

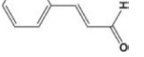

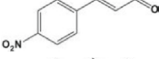
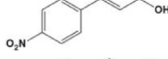

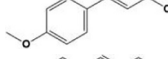
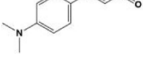
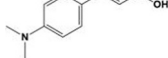
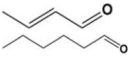
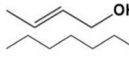
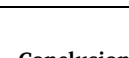

3.6. The universality of the obtained photocatalytic mechanism

Except for the HMF sample, a series of other α,β -unsaturated aldehydes can also be transformed into the corresponding α,β -unsaturated alcohol over the PtNi/TiO₂ photocatalyst under the optimized conditions with high conversion efficiency and product selectivity, as presented in Table 2. PtNi/TiO₂ exhibits a much higher photocatalytic activity toward aromatic unsaturated aldehydes (entries 1–8) than aliphatic unsaturated aldehydes (entries 9 and 10), which may result from the conjugation effects of the unsaturated carbon bonds [18].

Standard reaction conditions: 50 mg of samples, 100 mL of HMF aqueous solution (5 mM) containing 25 mL CH₃OH, a 300 W Xe lamp ($\lambda = 320\text{--}780$ nm), 5 h.

Table 2

Selective photocatalytic hydrogenation of α, β -unsaturated aldehydes over a PtNi/TiO₂.

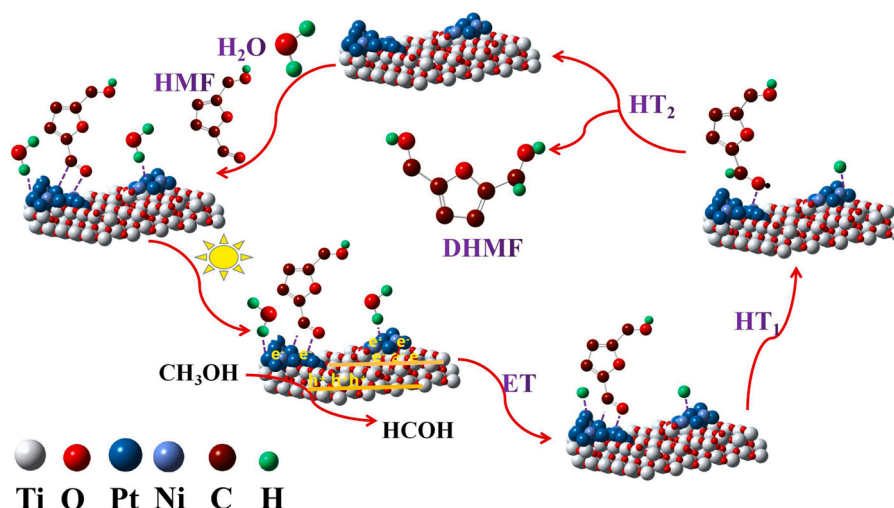
Reactant	Main product	Conversion (μmol)	Selectivity (%)
		100.0	100.0
		100.0	99.7
		100.0	100.0
		100.0	100.0
		99.2	99.8
		98.5	98.1
		90.3	88.9
		98.3	97.5
		85.5	78.9
		80.1	77.5

4. Conclusions

By performing EXAFS and in-situ characterizations, the interfacial interaction between PtNi cocatalyst and TiO₂ is verified. Benefiting from the strong electronic coupling of metal-semiconductor induced by interfacial bonding, the charge migration and HMF hydrogenation ability have significantly improved. in situ ATR-FTIR results further reveal that the significantly enhanced η^2 (C, O) aldehyde adsorption configuration of HMF molecules form DHMF via the CH-O-immediate route. This case not only provides a fundamental understanding of the underlying interfacial electronic-activity relationship, but also offers new insight for designing and fabricating highly efficient catalysts for photocatalytic selective conversion of high value-added chemicals.

CRediT authorship contribution statement

E. Cui, X. Yang and Y. Zhang conceived the idea of PtNi/TiO₂



Scheme 1. Schematic diagram of the photocatalytic HMF hydrogenation pathway over PtNi/TiO₂.

photocatalyst for HMF hydrogenation; E. Cui and X. Wang conducted the most of material fabrication and photocatalytic measurement; N. Xu provided the DFT calculation data; F. Zhang and G. Hou carried out the SAG measurement; M. Xie carried out the DRIFT measurement; Q. Li and Z. Wang contributed to the XPS measurement; E. Cui and Y. Zhang wrote this manuscript. All authors read and approved the final manuscript.

Declaration of Competing Interest

The authors declare that they have no known competing financial interests or personal relationships that could have appeared to influence the work reported in this paper.

Data Availability

Data will be made available on request.

Acknowledgements

This work is supported by the National Natural Science Foundation of China (NSFC, grant Nos. 22171239, 21771158, 21775136, and 52072330, 22072168), the Natural Science Foundation of Jiangsu Province (BK20221406) and Jiangsu Key Research and Development Project for Social Development Program (BE2022772). The authors gratefully acknowledge the Analysis and Test Center of YCIT for the structural characterizations.

Appendix A. Supporting information

Supplementary data associated with this article can be found in the online version at [doi:10.1016/j.apcatb.2023.122560](https://doi.org/10.1016/j.apcatb.2023.122560).

References

- H.L. Qian, Q.D. Hou, W.J. Zhang, Y.F. Nie, R.T. Lai, H.R. Ren, G.J. Yu, X.Y. Bai, H. Z. Wang, M.T. Ju, Construction of electron transport channels and oxygen adsorption sites to modulate reactive oxygen species for photocatalytic selective oxidation of 5-hydroxymethylfurfural to 2, 5-diformylfuran, *Appl. Catal. B: Environ.* 319 (2022), 121907.
- C. Li, J. Li, L. Qin, P.P. Yang, D.G. Vlachos, Recent advances in the photocatalytic conversion of biomass-derived furanic compounds, *ACS Catal.* 11 (2021) 11336–11359.
- L.I. Granone, F. Sieland, N. Zheng, R. Dillert, D.W. Bahnemann, Photocatalytic conversion of biomass into valuable products: a meaningful approach, *Green. Chem.* 20 (2018) 1169–1192.
- S. Chen, R. Wojcieszak, F. Dumeignil, E. Marceau, S. Royer, How catalysts and experimental conditions determine the selective hydroconversion of furfural and 5-hydroxymethylfurfural, *Chem. Rev.* 118 (2018) 11023–11117.
- S.X. He, Y.X. Chen, X. Li, L.X. Zeng, M.S. Zhu, Heterogeneous photocatalytic activation of persulfate for the removal of organic contaminants in water: a critical review, *ACS EST Eng.* 2 (2022) 527–546.
- E.J. Garcia-Suarez, D. Paolicchi, H. Li, J. He, S. Yang, A. Riisager, S. Saravanamurugan, Pd-catalysed formation of ester products from cascade reaction of 5-hydroxymethylfurfural with 1-hexene, *Appl. Catal. A: Gen.* 569 (2019) 170–174.
- J.H. Zhang, Z.H. Qi, Y. Liu, J.N. Wei, X. Tang, L. He, L.C. Peng, Selective hydrogenation of 5-hydroxymethylfurfural into 2,5-bis-(hydroxymethyl)furan over a cheap carbon-nanosheets-supported Zr/Ca bimetallic catalyst, *Energy Fuel* 34 (2020) 8432–8439.
- P. Mäki-Arvela, D. Ruiz, D. Yu. Murzin, Catalytic hydrogenation/hydrogenolysis of 5-hydroxymethylfurfural to 2,5-dimethylfuran, *ChemSusChem* 14 (2021) 150–168.
- B.L. Chen, Y.C. Feng, R.J. Huang, S.B. Yang, Z. Li, J. Sperry, S.L. Yang, X. Tang, Y. Sun, L. Lin, X.H. Zeng, Efficient synthesis of the liquid fuel 2,5-dimethylfuran from biomass derived 5-(chloromethyl)furfural at room temperature, *Appl. Catal. B: Environ.* 318 (2022), 121842.
- N.A. Endot, R. Junid, M.S.S. Jamil, Insight into biomass upgrade: a review on hydrogenation of 5-Hydroxymethylfurfural (HMF) to 2,5-Dimethylfuran (DMF), *Molecules* 26 (2021) 6848.
- M.S. Liu, T.Y. Peng, H.N. Li, L. Zhao, Y.H. Sang, Q.W. Feng, L. Xu, Y.Y. Jiang, H. Liu, J.M. Zhang, Photoresponsive nanostructure assisted green synthesis of organics and polymers, *Appl. Catal. B: Environ.* 249 (2019) 72–210.
- Y.Y. Guo, J.Z. Chen, Photo-induced reduction of biomass-derived 5-hydroxymethylfurfural using graphitic carbon nitride supported metal catalysts, *RSC Adv.* 6 (2016) 101968–101973.
- S.H. Dong, Z. Liu, R.H. Liu, L.M. Chen, J.Z. Chen, Y.S. Xu, light-induced catalytic transfer hydrogenation of aromatic aldehydes by palladium immobilized on amine-functionalized iron-based metal-organic frameworks, *ACS Appl. Nano. Mater.* 1 (2018) 4247–4257.
- Y.C. Li, J.L. Ma, D.N. Jin, G.J. Jiao, X.P. Yang, K.N. Liu, J.H. Zhou, R.C. Sun, Copper oxide functionalized chitosan hybrid hydrogels for highly efficient photocatalytic-reforming of biomass-based monosaccharides to lactic acid, *Appl. Catal. B: Environ.* 291 (2021), 120123.
- R.Q. Zhang, Y.Y. Liu, Z.Y. Wang, P. Wang, Z.K. Zheng, X.Y. Qin, X.Y. Zhang, Y. Dai, B.B. Huang, Selective photocatalytic conversion of alcohol to aldehydes by singlet oxygen over Bi-based metal-organic frameworks under UV–vis light irradiation, *Appl. Catal. B: Environ.* 254 (2019) 463–470.
- S.M. Qiao, Y.Y. Zhou, H.C. Hao, X.C. Liu, L. Zhang, W.Z. Wang, Selective hydrogenation via cascade catalysis on amorphous TiO₂, *Green. Chem.* 21 (2019) 6585–6589.
- A. Kumar, R. Ananthakrishnan, Strategic design of a WO₃/PdO_x carbon shell composite photocatalyst: visible light-mediated selective hydrogenation of 5-hydroxymethylfurfural, *ACS Appl. Energ. Mater.* 5 (2022) 2706–2719.
- C.H. Hao, X.N. Guo, Y.T. Pan, S. Chen, Z.F. Jiao, H. Yang, X.Y. Guo, Visible-light-driven selective photocatalytic hydrogenation of cinnamaldehyde over Au/SiC catalysts, *J. Am. Chem. Soc.* 138 (2016) 9361–9364.
- X.J. Wu, J.Q. Li, S.J. Xie, P.B. Duan, H.K. Zhang, J. Feng, Q.H. Zhang, J. Cheng, Y. Wang, Selectivity control in photocatalytic valorization of biomass-derived platform compounds by surface engineering of titanium oxide, *Chem* 6 (2020) 3038–3053.
- W. Guo, Y. Qin, C. Liu, B.B. Guo, J.H. Zou, Z.H. Xie, L. Wu, Unveiling the intermediates/pathways towards photocatalytic dechlorination of 3,3',4,4'-tetrachlorobiphenyl over Pd/TiO₂(B) nanosheets, *Appl. Catal. B: Environ.* 298 (2021), 120526.
- L.X. Yang, N.D. Feng, F. Deng, Aluminum-doped TiO₂ with dominant {001} facets: microstructure and property evolution and photocatalytic activity, *J. Phys. Chem. C* 126 (2022) 5555–5563.
- A. Serra-Cayuela, M. Castellari, J. Bosch-Fusté, M. Riu-Aumatell, S. Buxaderas, E. López-Tamames, Identification of 5-hydroxymethyl-2-furfural (5-hmf) in cava sparkling wines by LC-DADMS/MS and NMR spectrometry, *Food Chem.* 141 (2013) 3373–3380.
- Y. Wang, Z.H. Qi, H. Liu, J.H. Zhang, L.C. Peng, Fabrication of zirconium-doped activated carbon by chemical activation for catalytic transfer hydrogenation of 5-hydroxymethylfurfural into 2,5-dihydroxymethylfuran, *Energy Fuel* 36 (2022) 13796–13807.
- Z.L. Shao, S.N. Zhang, X.F. Liu, H. Luo, C.J. Huang, H.Z. Zhou, Z.X. Wu, J. Li, H. Wang, Y.H. Sun, Maximizing the synergistic effect between Pt⁰ and Pt²⁺ in a confined Pt-based catalyst for durable hydrogen production, *Appl. Catal. B: Environ.* 316 (2022), 121669.
- Q. Chen, B. Wei, Y. Wei, P.B. Zhai, W. Liu, X.K. Gu, Z.L. Yang, J.H. Zuo, R.F. Zhang, Y.J. Gong, Synergistic effect in ultrafine PtNiP nanowires for highly efficient electrochemical hydrogen evolution in alkaline electrolyte, *Appl. Catal. B: Environ.* 301 (2022), 120754.
- Y.J. Zhang, H.Y. Hu, X.J. Huang, Y.P. Bi, Photo-controlled bond changes on Pt/TiO₂ for promoting overall water splitting and restraining hydrogen-oxygen recombination, *J. Mater. Chem. A* 7 (2019) 5938–5942.
- Z.Y. Chen, L. Liang, H. Yuan, H. Liu, P. Wu, M.L. Fu, J.L. Wu, P.R. Chen, Y.C. Qiu, D.Q. Ye, L.M. Chen, Reciprocal regulation between support defects and strong metal-support interactions for highly efficient reverse water gas shift reaction over Pt/TiO₂ nanosheets catalysts, *Appl. Catal. B: Environ.* 298 (2021), 120507.
- Z. Li, Z.Y. Qi, S.W. Wang, T. Ma, L. Zhou, Z.W. Wu, X.C. Luan, F.Y. Lin, M.D. Chen, T. Miller, H.L. Xin, W.Y. Huang, Y. Wu, In-situ formed Pt₃Ti nanoparticles on a two-dimensional transition metal carbide (MXene) used as efficient catalysts for hydrogen evolution reactions, *Nano Lett.* 8 (2019) 5102–5108.
- X. Cheng, B. Xiao, Y.H. Chen, Y.S. Wang, L.R. Zheng, Y. Lu, H.Y. Li, G. Chen, Ligand charge donation-acquisition balance: a unique strategy to boost single Pt atom catalyst mass activity toward the hydrogen evolution reaction, *ACS Catal.* 12 (2022) 5970–5978.
- J.K. Zhang, X.H. Zheng, W.L. Yu, X. Feng, Y. Qin, Unravelling the synergy in platinum-nickel bimetal catalysts designed by atomic layer deposition for efficient hydrolytic dehydrogenation of ammonia borane, *Appl. Catal. B: Environ.* 306 (2022), 121116.
- K.L. Ding, A. Gulec, A.M. Johnson, N.M. Schweitzer, G.D. Stucky, L.D. Marks, P. C. Stair, Identification of active sites in CO oxidation and water-gas shift over supported Pt catalysts, *Science* 350 (2015) 189–192.
- M. Carosso, T. Fovanna, A. Richebueno, E. Vottero, M. Manzoli, S. Morandi, R. Pellegrini, A. Piovano, D. Ferri, E. Groppo, Gas phase vs. liquid phase: monitoring H₂ and CO adsorption phenomena on Pt/Al₂O₃ by IR spectroscopy, *Catal. Sci. Technol.* 12 (2022) 1359.
- M.A. Salaev, A.A. Salaeva, T.S. Kharlamova, G.V. Mamontov, Pt-CeO₂-based composites in environmental catalysis: a review, *Appl. Catal. B: Environ.* 295 (2021), 120286.
- J.Z. Chen, L.P. Zhang, Z.H. Lam, H.B. Tao, Z.P. Zeng, H.B. Yang, J.Q. Luo, L. Ma, B. Li, J.F. Zheng, S.P. Jia, Z.J. Wang, Z.P. Zhu, B. Liu, Tunneling for promoting overall water splitting and restraining hydrogen-oxygen recombination, *J. Am. Chem. Soc.* 138 (2016) 3183–3189.
- J.C. Liu, S.M. Xu, Y.F. Li, R.K. Zhang, M.F. Shao, Facet engineering of WO₃ arrays toward highly efficient and stable photoelectrochemical hydrogen generation from natural seawater, *Appl. Catal. B: Environ.* 264 (2020), 118540.
- W.L. Zhong, C. Wang, H.L. Zhao, S.Q. Peng, Z.P. Tian, R.Y. Shu, Y. Chen, Synergistic effect of photo-thermal catalytic glycerol reforming hydrogen production over 2D Au/TiO₂ nanoflakes, *Chem. Eng. J.* 446 (2022), 137063.

- [37] R.G. Kurniawan, N. Karanwal, J. Park, D. Verma, S.K. Kwak, S.K. Kim, J. Kim, Direct conversion of furfural to 1,5-pentanediol over a nickel-cobalt oxide-alumina trimetallic catalyst, *Appl. Catal. B: Environ.* 320 (2023), 121971.
- [38] H.J. Shi, Y.L. Wang, C.J. Tang, W.K. Wang, M.C. Liu, G.H. Zhao, Mechanism investigation on the enhanced and selective photoelectrochemical oxidation of atrazine on molecular imprinted mesoporous TiO₂, *Appl. Catal. B: Environ.* 246 (2019) 50–60.
- [39] K.X. Ke, W.M. Wan, J.G. Chen, Reaction pathways of furfural, furfuryl alcohol and 2-methylfuran on Cu(111) and NiCu bimetallic surfaces, *Surf. Sci.* 652 (2016) 91–97.
- [40] H. Ishikawa, M. Sheng, A. Nakata, K. Nakajima, S. Yamazoe, J. Yamasaki, S. Yamaguchi, T. Mizugaki, T. Mitsudome, Air-stable and reusable cobalt phosphide nanoalloy catalyst for selective hydrogenation of furfural derivatives, *ACS Catal.* 11 (2) (2021) 750–757.
- [41] W. Liu, Y.S. Yang, L.F. Chen, E.Z. Xu, J.M. Xu, S. Hong, X. Zhang, M. Wei, Atomically-ordered active sites in NiMo intermetallic compound toward low-pressure hydrodeoxygenation of furfural, *Appl. Catal. B: Environ.* 282 (2021), 119569.
- [42] X.J. Wu, J.Q. Li, S.J. Xie, P.B. Duan, H.K. Zhang, J. Feng, Q.H. Zhang, J. Cheng, Y. Wang, Selectivity control in photocatalytic valorization of biomass-derived platform compounds by surface engineering of titanium oxide, *Chem* 11 (2020) 3038–3053.
- [43] J.X. Fan, X.X. Yue, Y.N. Liu, D.Q. Li, J.T. Feng, An integration system derived from LDHs for CO₂ direct capture and photocatalytic coupling reaction, *Chem. Catal.* 2 (2022) 531–549.
- [44] H.V. Thang, S. Tosoni, L. Fang, P. Bruijninx, G. Pacchioni, Nature of sintering-resistant, single-atom Ru species dispersed on zirconia-based catalysts: a DFT and FTIR Study of CO adsorption, *ChemCatChem* 10 (2018) 2634–2645.
- [45] R.J. Chimentão, H. Oliva, J. Belmar, K. Morales, P. Mäki-Arvela, J. Wärnå, D. Y. Murzin, J.L.G. Fierro, J. Llorca, D. Ruiz, Selective hydrodeoxygenation of biomass derived 5-hydroxymethylfurfural over silica supported iridium catalysts, *Appl. Catal. B: Environ.* 241 (2019) 270–283.
- [46] A. Khan, M. Puttegowda, P. Jagadeesh, H.M. Marwani, A.M. Asiri, A. Manikandan, A.A.P. Khan, G.M. Ashraf, S.M. Rangappa, S. Siengchin, Review on nitride compounds and its polymer composites: a multifunctional material, *J. Mater. Res. Technol.* 18 (2022) 2175.
- [47] Y.J. Yang, D.X. Wu, R.S. Li, P. Rao, J. Li, P.L. Deng, J.M. Luo, W. Huang, Q. Chen, Z.Y. Kang, Y.J. Shen, X.L. Tian, Engineering the strong metal support interaction of titanium nitride and ruthenium nanorods for effective hydrogen evolution reaction, *Appl. Catal. B: Environ.* 317 (2022), 121796.
- [48] S.Q. Liu, W.L. Qi, S. Adimi, H.C. Guo, B. Weng, J.P. Attfield, M.H. Yang, Titanium nitride-supported platinum with metal-support interaction for boosting photocatalytic H₂ evolution of indium sulfide, *ACS Appl. Mater. Interfaces* 13 (2021) 7238–7247.
- [49] Y.H. Lin, Y. Yan, W. Peng, X.F. Qiao, D. Huang, H.W. Ji, C.C. Chen, W.H. Ma, J. C. Zhao, Crucial effect of TiH for promoting overall water splitting and restraining hydrogen-oxygen recombination, *J. Phys. Chem. Lett.* 11 (2020) 3941–3946.
- [50] X.Y. Xie, P. Xiao, W.H. Fang, G.L. Cui, W. Thiel, Probing photocatalytic nitrogen reduction to ammonia with water on the rutile TiO₂ (110) surface by first-principles calculations, *ACS Catal.* 9 (2019) 9178–9187.
- [51] S.J. Xie, Z.B. Shen, J. Deng, P. Guo, Q.H. Zhang, H.K. Zhang, C. Ma, Z. Jiang, J. Cheng, D.H. Deng, Y. Wang, Visible light-driven CH activation and C-C coupling of methanol into ethylene glycol, *Nat. Commun.* 9 (2018) 1181.